Journal of Applied Physics

RESEARCH ARTICLE | MARCH 24 2025

Measurement of near-wall microparticle motion induced by evanescent-field radiation pressure

Reiko Kuriyama ; Miyu Inoue; Daiki Arita; Kazuya Tatsumi

J. Appl. Phys. 137, 123105 (2025)
https://doi.org/10.1063/5.0239703

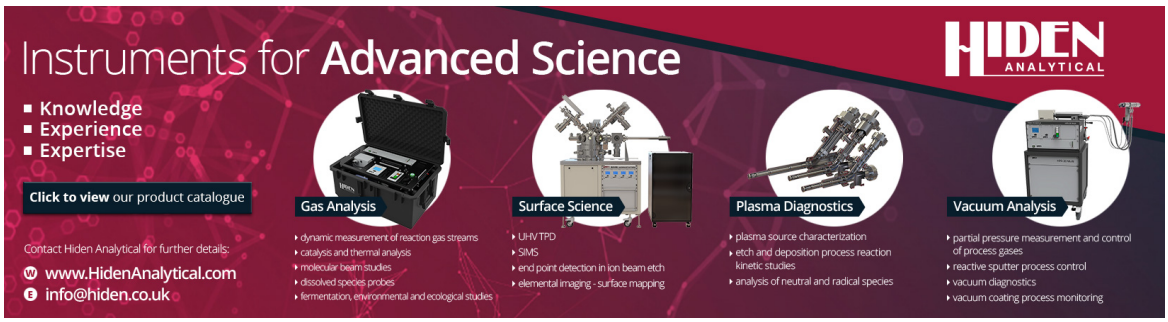

AIP Publishing

Journal of Applied Physics ARTICLE pubs.aip.org/aip/jap

Measurement of near-wall microparticle motion induced by evanescent-field radiation pressure

Cite as: J. Appl. Phys. **137**, 123105 (2025); doi: 10.1063/5.0239703
Submitted: 21 September 2024 · Accepted: 17 February 2025 ·
Published Online: 24 March 2025

Reiko Kuriyama,[1,a)] Miyu Inoue,[1] Daiki Arita,[1] and Kazuya Tatsumi[1,2]

AFFILIATIONS

[1]Department of Mechanical Engineering and Science, Graduate School of Engineering, Kyoto University, Kyoto daigaku-katsura, Nishikyo-ku, Kyoto 615-8540, Japan
[2]Department of Mechanophysics, Graduate School of Science and Technology, Kyoto Institute of Technology, Matsugasaki, Sakyo-ku, Kyoto 606-8585, Japan

[a)]**Author to whom correspondence should be addressed:** kuriyama.reiko.2m@kyoto-u.ac.jp

ABSTRACT

This study confirmed through experimental and theoretical investigations that considering the influences of the neighboring wall on the particle motion due to intermolecular, electrostatic, and hydrodynamic interactions is crucial when studying microparticles' motion under evanescent-field radiation pressure. The velocity of polystyrene microparticles parallel to the interface was measured in the evanescent field generated at a glass–solution interface. The measured velocity and the estimated radiation force increased with the laser power, decreased rapidly as the incident angle increased from the critical angle and almost overlapped for p- and s-polarizations as reported in previous studies, and scaled with the integrated evanescent intensity over the particle surface. The theoretical estimation of the equilibrium wall–particle separation distance d_{eq} revealed that the increase in the NaCl concentration from 0 to 60 mM caused a decrease in d_{eq} from 63 to 10 nm by reducing the repulsive electric double-layer force between the wall and particles through electrostatic screening. This reduction in d_{eq} increased both the evanescent-field radiation force and hydrodynamic drag force exerted on the particle and significantly affected the resultant near-wall particle velocity. The measured velocity was constant at $20 < d_{eq} < 70$ nm and rapidly decreased for $d_{eq} < 20$ nm, which was consistent with the theoretical model based on the balance between the radiation force and the modified Stokes drag force. These findings suggest that the motion of near-wall microparticles can be accurately predicted or controlled by appropriately incorporating the wall effect.

I. INTRODUCTION

An evanescent field is a thin layer of electromagnetic field generated by the total internal reflection (TIR) of light, which propagates only in the direction parallel to the interface and decays rapidly in the direction normal to the interface.[1,2] The length scale of intensity decay is typically of the order of the incident wavelength or smaller. Thus, the field can be regarded as a non-propagating light localized on the material surface. The evanescent field generates many notable phenomena in interaction with materials, such as the excitation of surface plasmon polaritons[3] and energy transfer through the optical tunneling effect.[4,5] The radiation pressure generated by evanescent fields is also an interesting phenomenon, which can be used for optical manipulation. Like in optical tweezers,[6–10] two types of radiation forces, namely, the scattering and gradient forces, act on objects in the evanescent field. Therefore, the scattering force propels the near-wall particles parallel to the TIR interface and, simultaneously, the gradient force pushes them normal to the interface, usually toward the interface (for particles with a higher refractive index than the surroundings).

Kawata and Sugiura first demonstrated the movement of polystyrene (PS) and glass microparticles parallel to the surface of a sapphire prism in water by using an evanescent field.[11] The maximum velocity of a PS particle of 6.8 μm diameter was 18 μm/s, which corresponded to the radiation pressure of approximately 1 pN. Later, similar phenomena were observed in the evanescent fields generated with a channel waveguide,[12–14] an objective lens with a high numerical aperture,[15] and optical fiber.[16] Theoretical calculations were performed by several groups. Chang[17] used the Mie–Debye theory to predict the optical force on a sphere caused by the evanescent field of a focused Gaussian beam. By applying

electromagnetic wave theory and the formalism proposed by Barton *et al.*,[18] Almaas and Brevik[19] calculated the optical force on a micrometer-sized sphere in the evanescent field of a plane wave. The Walz group[20,21] proposed a ray optics approach to calculate the radiation force and torque of an evanescent field exerted on micrometer-sized or larger particles and estimated the resultant particle velocity parallel to the interface.

These experimental and theoretical studies have revealed that the evanescent field can exert a radiation pressure in the pN range on near-wall microparticles and accelerate them simultaneously parallel to the interface at a speed on the order of 1 μm/s. A typical value for evanescent-field radiation pressure per unit laser power density is on the order of several tens of pN·μm^2/mW, which is comparable in magnitude to the typical value obtained with conventional optical tweezers.[22,23] Following these fundamental studies, various types of particle manipulation, such as sorting, trapping, patterning, and rotating, have been reported using counter-propagating evanescent fields.[24–28] There have also been research into enhancing the radiation pressure using resonance phenomena,[29–33] as well as research into applications in biomedicine[34] and optfluidics.[35] Furthermore, recent works are devoted to the manipulation of nanoparticles.[28,34,36–38] These studies present the potential application of evanescent-field radiation pressure to various types of non-contact manipulation of micro- and nano-objects next to the surface, which can prove useful in high-sensitivity analysis of minute samples in lab-on-a-chip applications, and for bottom-up fabrication technology for functional surface creation.

Accurately predicting the position and velocity of near-wall particles in the evanescent field is crucial for realizing aforementioned manipulations. However, evaluating only evanescent-field radiation pressure is not sufficient. The effects of other forces, especially the wall effects, should be considered in the analysis. This can be observed from experiments by the Walz group,[21] who measured the velocity of microparticles parallel to the interface in the evanescent field. In their experiments, the difference in the measured velocity between particles was as much as 100%. They speculated that one of the primary reasons for this large variation was the difference in the wall–particle separation distance, which highly depends on the interaction forces between the wall and particle, especially the electrostatic repulsive force. Because the evanescent-field intensity decays in the height direction, the wall–particle separation distance considerably influences the magnitude of the radiation pressure. Furthermore, the separation distance also influences the magnitude of hydrodynamic resistance exerted on near-wall moving particles. Both these change the resultant particle velocity, which was shown by Marchington *et al.*[15] through simulation.

The wall–particle separation distance is a crucial factor in accurately predicting and controlling the particle velocity in an evanescent field and depends on the interaction between the particle and the wall surface. However, studies have yet to examine the effects of various experimental conditions on the wall–particle separation distance in the evanescent field and have experimentally evaluated the effects of the separation distance on the particle velocity. Therefore, this study addresses the theoretical estimation of the wall–particle separation distance by considering the balance of various forces acting on the particles in the direction perpendicular to the interface. Considering the results of this estimation, we experimentally measure the near-wall particle velocity parallel to the interface by using a prism-based TIR microscopy system and investigate the dependence of the velocity on the wall-particle separation distance. The theoretical and experimental aspects addressed in this study are summarized as follows:

(1) The effects of experimental conditions on the equilibrium separation distance between the wall and the particle are theoretically investigated for PS microparticles in the evanescent field near the glass–water interface. The equilibrium separation distance is estimated by considering the balance between the gravitational force, van der Waals force, electric double layer (EDL) interaction force, and radiation force acting perpendicular to the interface (in Sec. IV A).
(2) The motion of PS particles is observed in Sec. IV B, and the particle velocity parallel to the glass–solution interface is measured in the subsequent sections. To demonstrate the validity of the experimental system and method using a home-built TIR microscope, the effects of incident-light conditions (laser power, polarization direction, and incident angle) on the particle velocity are investigated in Sec. IV C. Furthermore, the velocity of the microparticles of various diameters is measured in Sec. IV D to examine the effect of particle size on the velocity measurement. The measurement results are compared with those of previous studies and the predicted values are based on integrated evanescent intensity.
(3) The effect of the equilibrium separation distance on the particle velocity is experimentally investigated by changing the ion concentration of solution. The measured velocity is compared with the theoretical prediction derived by considering the changes in the radiation and hydrodynamic forces with respect to the separation distance (in Sec. IV E).

This study focuses on the experimental conditions that can considerably affect the wall–particle separation distance, and clarify the dependence of particle velocity on the separation distance and the type of force balance that determines this dependence. Therefore, the findings of this study can deepen our understanding of near-wall particle motion in an evanescent field and contribute to achieve accurate prediction and control of particle motion. To accurately measure the particle velocity, this study focused on experiments using microparticles and did not target nanoparticles, which are more difficult to clearly visualize because of the reduced contrast and intense Brownian motion.

II. THEORY

A. Evanescent field

Here, we consider the case in which light passes from one medium (with a higher refractive index n_1) to another (with a lower refractive index n_2), as illustrated in Fig. 1. If the incident angle θ_i exceeds the critical angle θ_c [$=\sin^{-1}(n_2/n_1)$], all the light is reflected. Even in this case, however, the electric field penetrates the interface and propagates parallel to the surface (toward the positive x-direction in Fig. 1). The intensity of the evanescent field, I_e, decays exponentially with perpendicular distance z from the

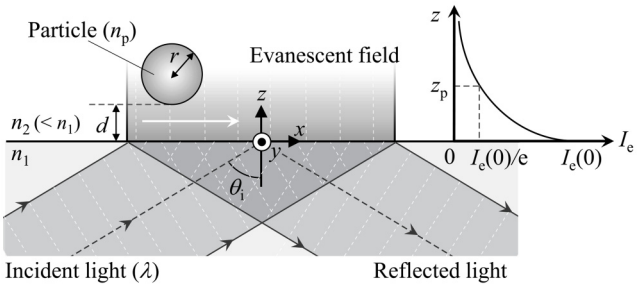

FIG. 1. Schematic of geometry and the coordinate system. A spherical particle of radius r and refractive index n_p is located in the evanescent field at a distance, d, from the interface. A laser beam of wavelength λ is incident from the first medium with refractive index n_1 to the interface at an angle of θ_i and is totally reflected. The graph on the right side of the figure shows the intensity distribution of the evanescent field along the z axis.

interface as follows:[1,2]

$$I_e(z) = I_e(0)\exp(-z/z_p), \tag{1}$$

where

$$z_p = \frac{\lambda_i}{4\pi\sqrt{n_1^2\sin^2\theta_i - n_2^2}}. \tag{2}$$

Here, $I_e(0)$ denotes the intensity of the evanescent field at the interface ($z = 0$). The characteristic length, z_p, is called the penetration depth, and λ_i is the wavelength of the incident light in vacuum. Because z_p is generally of the order of λ_i or smaller, the evanescent field is localized only in the near-wall area. For example, z_p is ~100 nm when visible light is totally reflected at the glass–water interface at an angle that is sufficiently larger than θ_c.

B. Radiation force of evanescent field

Here, we consider a radiation force acting on a dielectric sphere of radius r and refractive index n_p in a fluid with refractive index n_f. For the microparticles targeted in the present study (in the Mie regime), the Lorenz–Mie scattering theory provides a suitable description. In this case, the optical pressure can be derived in terms of Maxwell's stress tensor based on the detailed calculation of the electromagnetic field. However, to intuitively understand the origin and direction of the radiation pressure experienced by particles in the evanescent field, introducing a theoretical description in the Rayleigh regime, that is, a description based on the dipole approximation is useful. Therefore, in this section, the radiation pressure was analyzed based on the simple expressions obtained in the Rayleigh regime as follows. However, this provides only qualitative prediction for the microparticles targeted in this study.

The radiation force exerted on a particle by an electromagnetic field, F_{opt}, can be expressed in terms of two components,[23,39]

$$\boldsymbol{F}_{opt} = \frac{\sigma_{scat}\langle \boldsymbol{S}\rangle}{c/n_f} + \frac{1}{2}\alpha\nabla\langle \boldsymbol{E}^2\rangle, \tag{3}$$

where c is the speed of light, $\boldsymbol{S}$ is the Poynting vector, and $\boldsymbol{E}$ is the electric field-vector. The scattering cross section σ_{scat} is given by

$$\sigma_{scat} = \frac{8}{3}\pi k^4 r^6 \left(\frac{m^2-1}{m^2+2}\right)^2, \tag{4}$$

where k is the wave number in the medium ($k = 2\pi/\lambda$, where λ is the wavelength in the fluid) and $m = n_p/n_f$ is the relative refractive index of the particle. The particle polarizability, α, in Eq. (3) is defined by the Clausius–Mossotti relation as follows:

$$\alpha = 4\pi\varepsilon_0 n_f^2 r^3 \left(\frac{m^2-1}{m^2+2}\right), \tag{5}$$

where ε_0 is the electric permittivity of vacuum. The first term on the right-hand side of Eq. (3) is called the scattering force, $\boldsymbol{F}_{scat}$, which arises from the momentum transfer from the field to the particle via scattering. $\boldsymbol{F}_{scat}$ points in the direction of $\boldsymbol{S}$, i.e., in the field propagation direction. The second term is the gradient force, $\boldsymbol{F}_{grad}$, which arises from the potential energy of a dipole in the electric field. $\boldsymbol{F}_{grad}$ operates along the gradient of the electric-field intensity. If α is positive, i.e., the particle has a higher refractive index than the surrounding fluid ($n_P > n_f$), $\boldsymbol{F}_{grad}$ acts toward the high-intensity region of the electric field. Since the evanescent field propagates parallel to the surface and its intensity decays with increasing distance from the surface, the particle in the evanescent field is pushed parallel to the surface by $\boldsymbol{F}_{scat}$ and attracted toward or repelled from the surface by $\boldsymbol{F}_{grad}$, depending on the relative refractive index of the particle. This qualitative conclusion regarding the direction of the evanescent-field radiation pressure obtained in the Rayleigh regime is consistent with those obtained in the Mie and ray optics regimes,[17,19–21] despite the differences in their theoretical treatments. Note that rotational torque as well as forces parallel and normal to the surface act on the particle;[20,21] however, those aspects are not addressed in this study. Furthermore, the effect of particle – particle interactions known as optical binding is not considered here. The effects of multiple reflections between the wall and particles on the scattering field can be ignored under the experimental conditions of this study.[40]

C. Balance of forces exerted on the particle

Figure 1 is a schematic of the geometry used in this study. We consider the situation in which a spherical particle is adjacent to a wall at a separation distance d in an aqueous solution. Generally, the material surface in contact with an aqueous solution can be charged by the protonation/deprotonation of the surface groups or adsorption of ions to the surface.[41] Therefore, the particle is subjected to three forces, namely, the gravitational force, F_G; van der Waals force, F_{vdW}; and the electric double-layer (EDL) interaction force, F_{EDL}. Furthermore, when an evanescent field is generated, radiation forces $F_{opt,x}$ and $F_{opt,z}$ are exerted on the particle in the x- and z-directions, respectively.

First, we discuss the balance of the abovementioned forces in the z-direction and derive the equilibrium distance between the particle and the wall, d_{eq}. If we take each force as positive in the positive z-direction, the total force acting on the particle in the

z-direction is

$$F_{\text{total}} = F_{\text{G}} + F_{\text{vdW}} + F_{\text{EDL}} + F_{\text{opt},z}. \tag{6}$$

Here,

$$F_{\text{G}} = -\frac{3}{4}\pi r^3 g(\rho_{\text{p}} - \rho_{\text{f}}), \tag{7}$$

where $g = 9.81\ \text{m/s}^2$ is the gravitational acceleration and ρ_{p} and ρ_{f} are the particle and fluid densities, respectively.

The F_{vdW} on a sphere near a planar surface can be calculated using the analytical expression derived by Hamaker.[42] When the retardation effect is included,

$$F_{\text{vdW}} = -\frac{A}{6}\left(\frac{r}{d^2} + \frac{r}{(d+2r)^2} - \frac{2r}{d(d+2r)}\right)\left(\frac{\lambda_{\text{L}}}{\lambda_{\text{L}} + sd}\right) + \frac{A}{6}\left(\frac{r}{d} + \frac{r}{d+2r} - \ln\frac{d}{d+2r}\right)\left(\frac{\lambda_{\text{L}}\, s}{(\lambda_{\text{L}} + sd)^2}\right), \tag{8}$$

where A denotes the Hamaker constant. The terms in Eq. (8) that contain the London characteristic wavelength λ_{L} and constant s are retardation-effect correction factors.[43,44]

The F_{EDL} between the particle and planar surface can be calculated by considering the limiting case of Hogg's analytical expression derived for two spherical particles using Derjaguin's method,[45]

$$F_{\text{EDL}} = 2\pi\varepsilon_0\varepsilon_{\text{f}} r\kappa\left(\zeta_{\text{p}}^2 + \zeta_{\text{w}}^2\right) \times \left[\frac{2\zeta_{\text{p}}\zeta_{\text{w}}}{\zeta_{\text{p}}^2 + \zeta_{\text{w}}^2}\left(\frac{\exp(-\kappa d)}{1 - \exp(-2\kappa d)}\right) - \left(\frac{\exp(-2\kappa d)}{1 - \exp(-2\kappa d)}\right)\right], \tag{9}$$

where ε_{f} is the relative permittivity of the fluid, κ is the Debye–Hückel parameter, and ζ_{p} and ζ_{w} are the zeta potentials of the particle and wall, respectively. For an electrolyte solution with symmetric ions,

$$\kappa = \left(\frac{2000 N_{\text{A}}\, z_{\text{i}}^2 e^2 C_\infty}{\varepsilon_0\varepsilon_{\text{f}} k_{\text{B}} T}\right)^{1/2}, \tag{10}$$

where N_{A} is the Avogadro constant, z_{i} is the ion valence, e is the elementary charge, C_∞ is the ion concentration in the bulk region (mol/l), and T is the absolute temperature. Here, κ^{-1} represents the EDL characteristic thickness and is generally 1−100 nm at $C_\infty = 10^{-1}$–10^{-5} mol/l at room temperature. Note that Eq. (9) is based on the Debye–Hückel approximation, which yields good approximations for small zeta potentials up to $|\zeta| \sim 60$ mV.[45]

In this study, $F_{\text{opt},z}$ was estimated based on a theoretical prediction suggested by Waltz.[20] Figure 9 of Ref. 20 shows the relationship between the particle radius and radiation force normalized by the characteristic momentum falling on the sphere, which was obtained under conditions similar to those of our experiments.

Under the experimental conditions of this study, F_{vdW} acted in the negative z-direction; i.e., it was attractive toward the wall. This was because the constant A adopted a positive value ($\sim 2.18 \times 10^{-21}$ J) for the PS–glass pair in water. This value was estimated using the relationship known as "combining laws"[46] and the known values for each material in vacuum.[47] F_{G} and $F_{\text{opt},z}$ were also negative because the density and refractive index of the particles (PS) exceeded those of the surrounding medium (water). By contrast, F_{EDL} functioned as a repulsive force because the PS particles and the glass wall used in this study were both negatively charged in the solution because of the dissociation of sulphonyl and silanol groups, respectively.

The particle reaches d_{eq} when $F_{\text{total}} = 0$. Once the equilibrium height is reached, the particle moves parallel to the wall surface at constant velocity U, which is determined by the balance between the horizontal forces as follows:

$$F_{\text{opt},x} + F_{\text{Stokes}} = 0, \tag{11}$$

where $F_{\text{opt},x}$ is the radiation force in the x-direction and F_{Stokes} is the Stokes drag force. If the particle is close to the wall (within the region $d/r < 1$), the drag force should be evaluated by the modified Stokes law using the correction term for the wall effect, R, which is given by[48]

$$F_{\text{Stokes, mod}} = -6\pi\mu r U R = -6\pi\mu r U\{-(8/15)\ln(d/r) + 0.9588\}. \tag{12}$$

Rotational torque and propulsive force act on the particles because of the non-uniform radiation pressure in the z-direction.[20,21] The approximate torque value estimated by referring to the numerical simulation results of a previous study[20] was 2×10^{-6} pNm under the typical experimental conditions used in this study. This yielded particles rotating around the y-axis so that the particle bottoms moved in the positive x-direction at approximately 0.65 rad/s (approximately 0.1 revolution per second). The drag force acting on such a rotating particle was estimated to be approximately 10% of that related to the translational motion and was neglected in the subsequent analysis. The effect of the rotational motion on the lift force in the z-direction was estimated to be sufficiently small (approximately 1×10^{-6} pN) and, thus, was not considered.

III. EXPERIMENTAL DETAILS

A. Apparatus

Figure 2(a) is a schematic of the experimental setup. A continuous-wave laser (Coherent, Genesis MX488-1000SLM) operating at 488 nm was used as the light source to generate an evanescent field. A linearly polarized laser beam was passed through a focusing lens and introduced horizontally into a trapezoidal prism (Sigmakoki, $n = 1.52$) mounted on a sample stage. Figure 2(b) is an enlarged view of the test section. The beam traveled through the prism and entered the cover glass of a prepared slide, which comprised bottom and upper cover glasses (Matsunami; C024601, $n = 1.52$) spaced by two strips of 120 μm-thick parafilm. Immersion oil (Leica; Type F, $n = 1.52$) was placed between the prepared slide and prism to achieve optical coupling. The beam underwent TIR at the interface between the cover glass and particle solution, generating an evanescent field in the solution. As the laser was in TEM_{00}

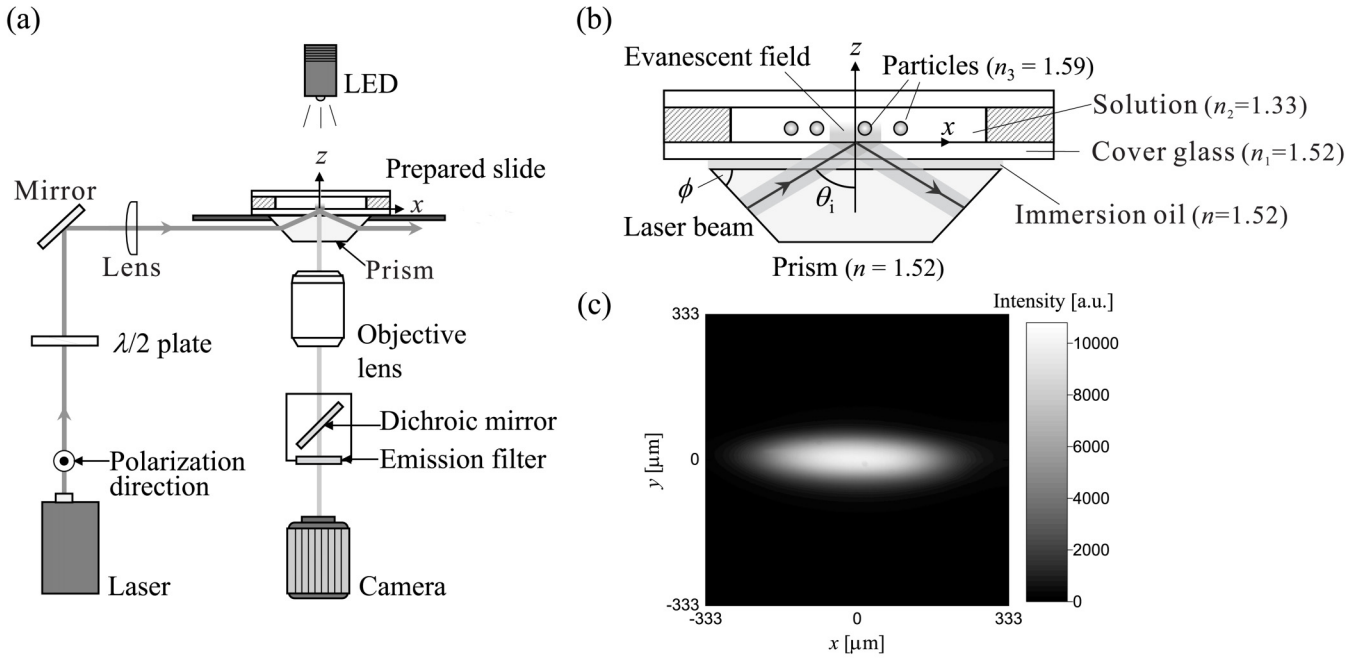

FIG. 2. (a) Schematic of the experimental setup and (b) enlarged view of the test section. The particle solution was enclosed in a prepared slide, which was placed on a trapezoidal prism of base angle ϕ and illuminated by an evanescent field generated at the glass–solution interface. (c) Intensity distribution in the x–y plane of the evanescent field visualized using fluorescent dye solution.

mode with a circular cross section, the area in which the evanescent field was generated (hereafter, the "evanescent spot") had an ellipsoidal shape with a Gaussian intensity profile, as shown in Fig. 2(c). In this study, three prisms with different base angles ϕ were used to investigate the effect of the TIR incident angle θ_i on the particle motion. The ϕ, θ_i, and z_p of each prism are summarized in Table I. An LED (Thorlabs; M565L3) was used as the illumination light to monitor the particle motion. Transmission images of the particles were collected using a home-built microscope system equipped with an objective lens (Olympus; LMPLFLN, 20x, $NA = 0.40$) and a CMOS camera (Andor Zyla; 4.2 PLUS, 2048 × 2048 pixels, 16 bits). A dichroic mirror (Semrock; FF506-Di03) and optical filter (Semrock; FF01-500/LP25) were used to remove the strongly scattered light at the laser wavelength. The acquired image had a resolution of 0.325 μm/pixel.

TABLE I. Base angle ϕ, TIR incident angle θ_i, and penetration depth z_p for each prism.

ϕ (deg)	θ_i (deg)	z_p (nm)
25	61.6	282
30	64.7	112
45	72.7	67

B. Particle solutions

Spherical PS particles of different diameters (Thermo Fisher Scientific; 4000 series mono-sized particles, $2r = 1$, 3, 5, 7, 10, and 12 μm) were used. The particle refractive index and density were 1.59 and 1.05 g/cm^3, respectively. These particles were separated from their original carrier fluid by centrifugation and suspended in an aqueous solution at low concentrations (in the range of 5×10^{-4}–1.5×10^{-1} wt. % depending on the particle size) to reduce the effects of particle–particle interactions, such as collisions, hydrodynamic interactions, and optical binding. The properties of the aqueous solutions are listed in Table II. Sodium chloride (NaCl) was added to pure water at various concentrations to adjust F_{EDL} on the particles by changing κ, ζ_p, and ζ_w in Eq. (9). Furthermore, uranine (Nacalai Tesque; #35816-92) and sodium lauryl sulfate (SLS, Nacalai Tesque; #31606-75) were added to all solutions at a constant concentration. Uranine was used to visualize the evanescent spot. SLS is an anionic surfactant that inhibits particle aggregation by adsorbing to the particle surface and decreasing ζ_p.[49] In the calculation of F_{EDL} using Eqs. (9) and (10), the ion concentration in the bulk C_∞ was assumed to be equal to the sum of the SLS and NaCl concentrations in the solution.

The electrophoretic mobilities of the 10 μm PS particles in each solution were measured using a zeta potential analyzer (Malvern Panalytical; Zetasizer Ultra ZSU5700) and converted to

TABLE II. Solute concentration, thickness of the electric double layer κ^{-1}; zeta-potentials of the microparticles and glass, ζ_p and ζ_w, respectively; and equilibrium separation distance d_{eq} in each solution used as carrier fluid.

	Concentration (mM)			κ^{-1}	ζ_p	ζ_w	d_{eq}
Solution	Uranine	SLS	NaCl	(nm)	(mV)	(mV)	(nm)
0	5×10^{-3}	3.5	0	5.2	−136	−74	63
1			1	4.6	−128	−71	55
5			5	3.3	−108	−62	39
10			10	2.6	−94	−56	30
15			15	2.2	−84	−52	24
20			20	2.0	−77	−49	21
40			40	1.5	−58	−41	14
60			60	1.2	−46	−36	10

the zeta potential based on the Henry equation. As the surfaces of the PS particles used in this study were modified with sulfonyl groups, the measured potentials exhibited large negative values in all solutions. The relationship between the ion concentration and the measured zeta potential was fitted using an empirical relation, in which the zeta potential scaled linearly with the negative logarithm of the counterion concentration[41] (the details are reported in the supplementary material). Table II summarizes the zeta potential of the PS particles estimated based on the above fitting results and the zeta potential of the glass wall estimated based on the experimental data in Ref. 41. Although some of these zeta-potential values are outside the valid range of the Debye–Hückel approximation, Eq. (9) was used to estimate F_{EDL} for all conditions presented here.

C. Procedures

Prior to the particle velocity measurements, the position and intensity profile of the evanescent field were measured by fluorescence imaging using a prepared slide filled with a 50 μM uranine solution. Figure 2(c) is a typical image of a fluorescent dye solution excited by an evanescent field. An ellipsoidal evanescent spot with Gaussian intensity distribution is apparent. The center position and $1/e^2$ size of the spot were evaluated by fitting a Gaussian function to the intensity distribution. Following fluorescence observation of the evanescent spot, another prepared slide filled with particle solution was observed. The prepared slide was left to stand for more than 5 min to allow the particles to settle on the bottom glass wall. Immediately after laser irradiation was initiated, 30 successive particle images were collected for 100 s at a 0.3 fps frame rate. Under each experimental condition, measurements were performed thrice, each time with a different sample.

The obtained particle images were processed using the open-source image processing software, ImageJ (ver. 1.51 k, National Institutes of Health, USA). First, background subtraction was performed to reduce the non-uniformity of the LED illumination. Black and white inversion was then performed, and the particles were detected and tracked automatically over 30 images using the TrackMate plugin. Instantaneous position and velocity data were obtained for each particle. Considering the particle velocity distribution in the evanescent spot (described in detail in Sec. IV B), the average particle velocity U_{ave} was evaluated in the following manner. Particles crossing the area where I_e was equal to or greater than 85% of the peak intensity were extracted. The maximum velocity in the 85% area was calculated for each particle. Finally, the average value of the maximum velocities of all particles in the three measurements, U_{ave}, was calculated. Furthermore, the standard deviation of the maximum velocities of all particles was used to estimate the 95% confidence interval, which was plotted on the graphs as an error bar for U_{ave} in Secs. IV C–IV E. The number of particles used to calculate U_{ave} was in the range of 8–45.

IV. RESULTS AND DISCUSSION

A. Estimation of equilibrium distance between wall and particle

This section reports estimation of d_{eq} based on the vertical force balance described in Sec. II C. The values listed in Table III were used as reference values unless otherwise mentioned. The particle was assumed to be located at the center of the evanescent spot; thus, $\boldsymbol{F}_{grad}$ in the x–y plane was ignored. Figures 3(a)–3(c) show the vertical forces acting on the PS particle as a function of d. The thin colored lines represent F_G, F_{vdW}, F_{EDL}, and $F_{opt,z}$. The thick black line represents F_{total}. The forces exerted on the PS particles with diameters $2r = 10$ and 1 μm in solution 0 ($C_{NaCl} = 0$ mM) are shown in Figs. 3(a) and 3(b), respectively, and those exerted on 10 μm PS particles in solutions with different C_{NaCl} concentrations are shown in Fig. 3(c).

TABLE III. Reference values for calculating vertical force acting on near-wall microparticles.

Parameter	Values
Particle diameter, $2r$ (μm)	10
Refractive index of particle, n_p (−)	1.59
Particle density, ρ_p (g/cm^3)	1.05
Fluid density, ρ_f (g/cm^3)	0.998
Hamaker constant, A (J)	2.18×10^{-21}
London characteristic wavelength, λ_L (m)	1.00×10^{-7}[26,27]
Constant related to retardation, s (-)	11.116[26,27]
Electric permittivity of vacuum, ε_0 (F/m)	8.85×10^{-12}
Relative permittivity of fluid, ε_f (-)	80.1
NaCl concentration, C_{NaCl} (mM)	0
EDL thickness, κ^{-1} (nm)	5.2
Particle zeta potential, ζ_p (mV)	−136
Wall zeta potential, ζ_w (mV)	−74
Absolute temperature, T (K)	295
Nondimensionalized radiation pressure (-)	−0.122[20]
Laser power (mW)	500
Beam diameter (μm)	140
Refractive index of wall, n_1 (-)	1.52
Refractive index of solution, n_2 (=n_f) (-)	1.33
Incident angle, θ_i (deg)	61.6
Light wavelength in vacuum, λ_0 (nm)	488
Penetration depth, z_p (nm)	283

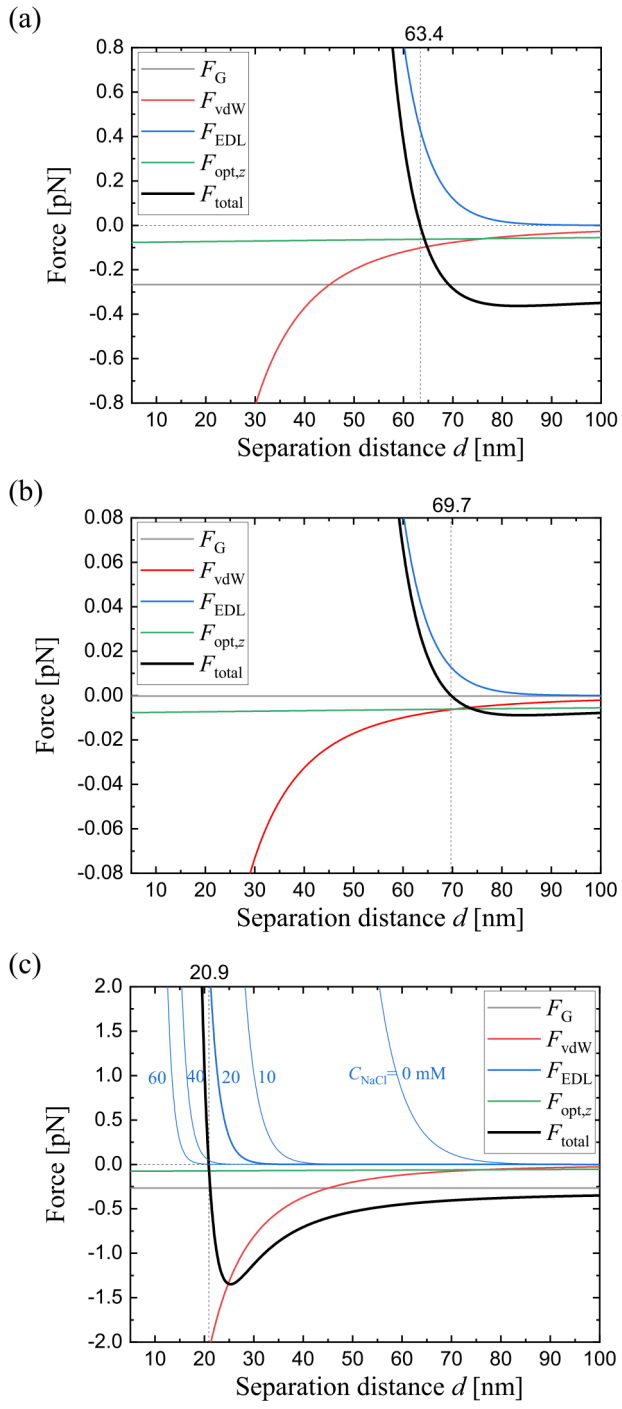

FIG. 3. Relationship between vertical forces acting on the PS particle and separation distance d for particles of diameter (a) $2r = 10\,\mu$m and (b) $2r = 1\,\mu$m in solution 0 ($C_{NaCl} = 0$ mM). (c) EDL interaction force, F_{EDL}, calculated for $10\,\mu$m PS particle in solutions of different NaCl concentrations, C_{NaCl}, ranging from 0 to 60 mM. The thick black line represents the total interaction force, F_{total}, for solution 20 ($C_{NaCl} = 20$ mM).

From Fig. 3(a), F_{vdW} and F_{EDL} acted as attractive and repulsive forces against the wall, respectively, and their magnitudes decreased rapidly with d. $F_{opt,z}$, which acted as an attractive force, decreased with d at the rate determined by z_p (282 nm in this case). Consequently, F_{total} exhibited a rapid change with d in the near-wall region ($d < 80$ nm in this case) and approached a constant equal to F_G at an infinite distance. The distance at which $F_{total} = 0$ corresponds to d_{eq}. In Fig. 3(a), for $2r = 10\,\mu$m, d_{eq} was 63.4 nm. Comparing the cases of the 10- and $1\,\mu$m particles [Figs. 3(a) and 3(b)], the magnitudes of F_{vdW}, F_{EDL}, and $F_{opt,z}$ on the $1\,\mu$m particle were approximately 10 times smaller than those on the $10\,\mu$m particle. The F_G magnitude for the $1\,\mu$m case was 1000 times smaller than that for the $10\,\mu$m case. As a result of the balance of those forces, d_{eq} was 69.7 nm in the case of the $1\,\mu$m particle, approximately 10% larger than that in the case of the $10\,\mu$m particle.

The blue lines in Fig. 3(c) show the F_{EDL} values in solutions with different C_{NaCl} ranging from 0 to 60 mM (case solutions 0 −60). The thick black line represents F_{total} for case solution 20 ($C_{NaCl} = 20$ mM) and d_{eq} was 20.9 nm in this case. The magnitude of F_{EDL} decreased with increasing C_{NaCl}. This was because both the zeta potentials and EDL thickness decreased as a result of electrostatic screening. The relationship between C_{NaCl} and d_{eq} for the $10\,\mu$m PS particles is reported in Fig. 4 and Table II, where d_{eq} decreased from 63 to 10 nm with increasing C_{NaCl} from 0 to 60 mM. The results for the 1- and $12\,\mu$m PS particles are also shown in Fig. 4. The difference in d_{eq} with particle size decreased with increasing C_{NaCl}.

From the above discussion, the ion concentration of the solution had the most significant effect on d_{eq}. The change in d_{eq} affects both $F_{opt,x}$ and $F_{Stokes,mod}$. $F_{opt,x}$ increases with decreasing d_{eq} because the evanescent field intensity acting on the particle

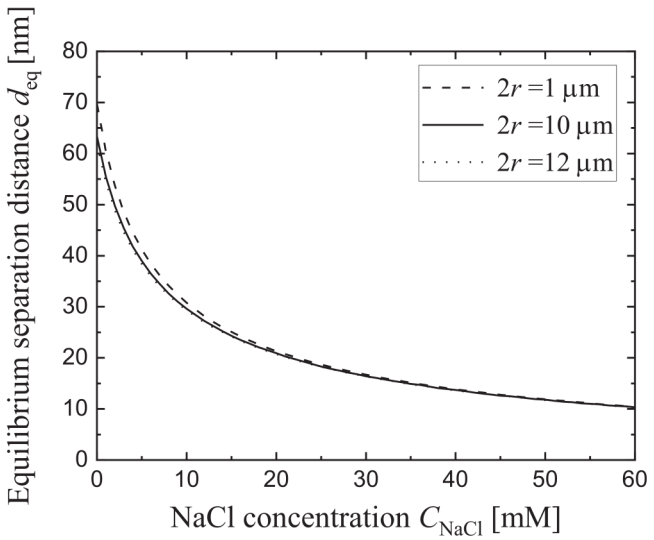

FIG. 4. Relationships between C_{NaCl} and equilibrium separation distance, d_{eq}, for 1-, 10-, and $12\,\mu$m PS particles. The calculated values of d_{eq} at the NaCl concentrations of solutions 0–60 for $10\,\mu$m particle are listed in Table II.

increases as the particle gets closer to the wall. At the same time, the wall effect on hydrodynamic resistance becomes more pronounced as d_{eq} decreases. Under the present experimental conditions, d_{eq} varied in the range of approximately 10–70 nm, and as a result, d_{eq}/r changed in the range of 0.002–0.14. This generated a change in the $F_{Stokes,mod}$ correction factor R [in Eq. (12)] from 4.3 to 2.7. Thus, the particles propelled parallel to the interface in the evanescent field were subjected to a hydrodynamic resistance that was several times larger than that in the bulk. In addition, the magnitude of the resistance varied by a factor of approximately two, depending on d_{eq}/r.

B. Observation of particle motion

This section reports observation of the motions of 12 μm PS particles in solution 0. Figure 5(a) is a raw transmission image of the particles at the beginning of the measurement ($t = 0$ s). The white ellipse indicates the position of the evanescent spot. The laser power, polarization, and θ_i at the glass–solution interface were 507 mW, s-polarization, and 62°, respectively. Figures 5(b) and 5(c) show the particle motions inside and outside the evanescent spot, respectively. The particles in the spot moved in the positive x-direction, i.e., the traveling direction of the evanescent wave [Fig. 5(b)], whereas the particles outside the spot exhibited only random, small-magnitude positional changes due to Brownian motion [Fig. 5(c)]. The particle velocity in Fig. 5(b) was of the order of 1 μm/s.

Figure 6(a) is a particle image processed using ImageJ software. The pink circles indicate the initial particle positions and the colored lines represent the particle trajectories for 100 s. Reference numbers have been added to some particles in the figure. The particles passing near the center of the evanescent spot had longer trajectories than those near the periphery; that is, the particles moved faster around the central region. Figure 6(b) shows the relationship between the x position and the particle velocity in the evanescent spot. The particles crossing near the center of the spot had trajectories with bell-like curves and a maximum velocity of 4–5 μm/s, whereas those around the periphery of the spot had only small velocities that fluctuated in the vicinity of 0–1 μm/s. In Fig. 6(c), the velocity distributions of some particles were normalized by their peak values and compared with the intensity distribution of the evanescent field shown by the black line. Although the velocity distributions had a slightly steeper slope, they agreed reasonably well with the Gaussian intensity distribution of the evanescent field. This outcome is attributed to the fact that the radiation pressure is proportional to the intensity of the electromagnetic field.

C. Effects of incident-light conditions on particle velocity

The particle velocity parallel to the glass–solution interface was measured under various conditions with different laser powers, polarizations, and θ_i using 10 μm PS particles. Solution 0 was used as working fluid because, among those listed in Table II, solution 0 yielded the largest d_{eq} and the friction between the wall and particle from affecting the particle motion can be prevented. The square symbols in Fig. 7 show the measured relationship between the laser power at the glass–solution interface and U_{ave}. The vertical axis on the right side shows the radiation pressure in the x-direction, $F_{opt,x}$, which was estimated using Eq. (12). Because the change in the incident light conditions has only small effect on d_{eq} (less than 1 nm) within the range of conditions in this study, d_{eq} was fixed at 63.4 nm for the force calculation. Therefore, the left and right axes

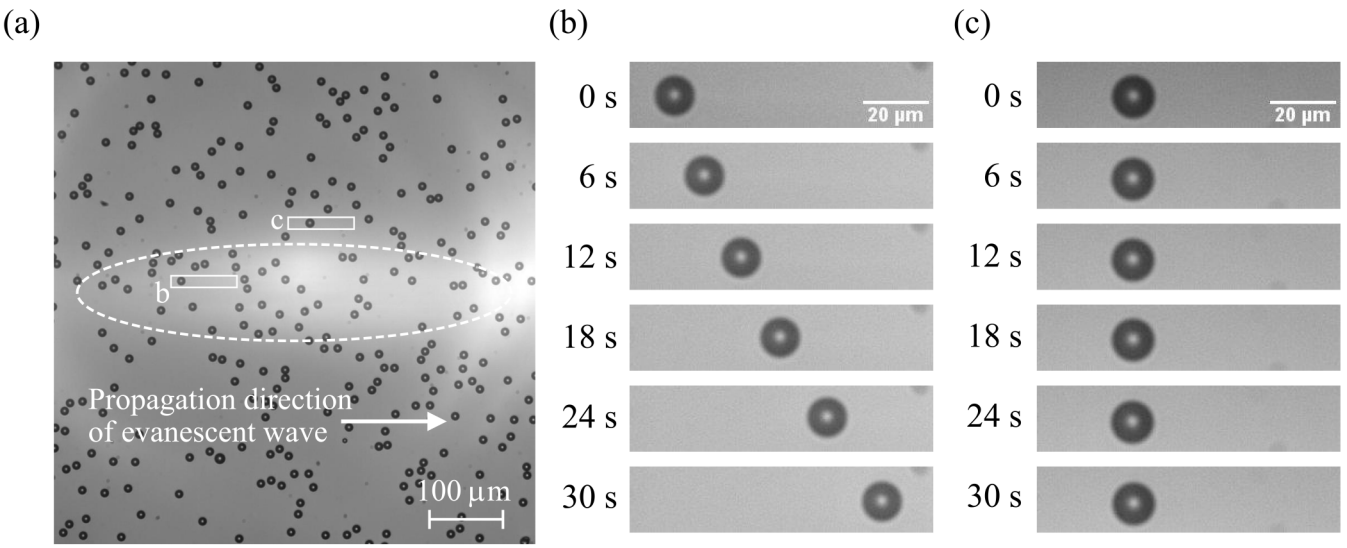

FIG. 5. (a) Transmission image of 12 μm PS particles in evanescent spot at measurement onset ($t = 0$ s). Time-series particle images in boxed areas indicated in Fig. 5(a), showing particle motion (b) inside and (c) outside of the evanescent spot.

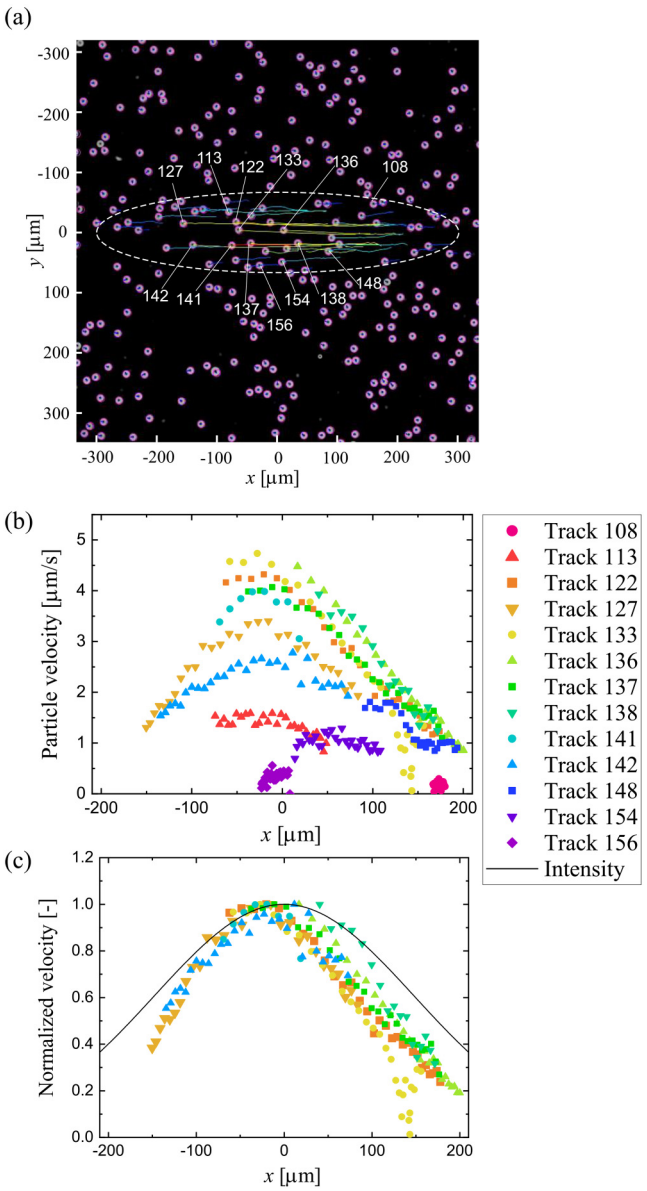

FIG. 6. (a) Superimposed image of the initial particle positions at $t = 0$ s and their trajectories during measurement time (100 s). (b) Relationship between particle position in the x direction and particle velocity for several particles in the evanescent spot. (c) Comparison of particle velocity distribution and evanescent-field intensity distribution (both normalized by peak values).

of the graph have a linear relationship. The non-zero particle velocity (~0.3 μm/s) at a 0 mW laser intensity was due to the Brownian motion of the particles. The colored dotted lines represent the integrated intensities of the evanescent field $I_{e,integrated}$ for each condition. $I_{e,integrated}$ is the area integral of the evanescent-field intensity in Eq. (1) over the entire microparticle surface. Theoretically, $F_{opt,x}$

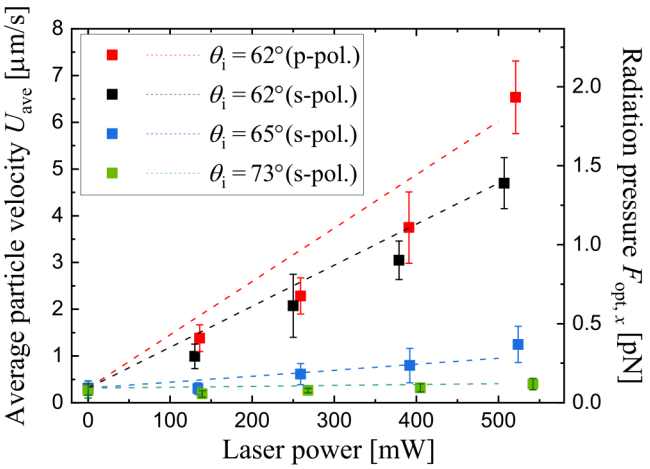

FIG. 7. Relationship between laser power at measurement section and average particle velocity, U_{ave}, of 10 μm PS particles in solution 0, measured at different incident angles, θ_i, and polarization directions. The vertical axis on the right shows the radiation force in the x-direction, $F_{opt,x}$, estimated based on the balance with $F_{Stokes,mod}$. The dotted lines represent the integrated evanescent-field intensity normalized by the value at 500 mW, s-polarization, $\theta_i = 62°$.

is expected to be proportional to $I_{e,integrated}$. For comparison with the measured results, $I_{e,integrated}$ was normalized by the measured value obtained at a laser power of 507 mW, for $\theta_i = 62$ and s-polarization.

The measured U_{ave} (and $F_{opt,x}$) increased with the laser power, as shown in Fig. 7, which is consistent with the previous experimental reports[15,20] and theoretical prediction based on $I_{e,integrated}$. However, the rate of increase in the measured particle velocity increased with increasing laser power, whereas the integrated intensity was proportional to the laser power. This trend agrees with Fig. 6(c), where the particle velocity varied more steeply with x than with the evanescent-field intensity. The cause of this phenomenon remains unclear. One possible cause is a decrease in the viscosity of the surrounding fluid due to heating by optical absorption, as noted in the previous study.[21] For example, if we assume that the water temperature increases by 10 K from the room temperature (295 K), the viscosity decreases by about 14%, which leads to an increase in the particle velocity of about 16%. However, due to the extremely low absorbance of water and glass at 488 nm (0.02 and 0.5 m^{-1}, respectively[50,51]), the temperature rise was estimated to be less than 1 K at most, referring to the method by Mao *et al.*[52] Thus, the temperature increase due to laser irradiation is not considered to be the main source of error in the present study.

The rate of increase in the measured velocity vs the laser power decreased significantly as the angle of incidence increased from θ_c (=61.0°), which agrees well with the theoretical prediction obtained using $I_{e,integrated}$. This is because both z_p and the light intensity at the glass–solution interface decreased when θ_i increased from θ_c. The measurement results agreed well with the previous experiments[11,29] and also with Walz calculation,[20] which reported that the radiation pressure decreased by approximately one order of magnitude when the angle of incidence was increased by ~5° from θ_c.

The measured U_{ave} for p- and s-polarization at $\theta_i = 62$ almost overlapped within the error bars except for those at the laser power of approximately 500 mW. This result is consistent with the calculation by Walz,[20] which revealed that the radiation pressure was larger for p-polarized light by a few percent under conditions similar to those of our experiment. By contrast, the difference in $I_{e,integrated}$ between p- and s-polarization was approximately 30%, which was larger than the difference in U_{ave} because the difference in $I_{e,integrated}$ due to polarization states is attributed solely to the difference in the evanescent intensity at interface $I_e(0)$. Therefore, $I_{e,integrated}$ is always larger for p-polarization.[22] However, studies have reported that many experimental factors (such as particle size, refractive index, wavelength, and incident angle) were relevant to which polarization state provided greater radiation pressure.[19,20] Therefore, discussing the difference between different polarization states only from $I_{e,integrated}$ values is difficult.

The measurement results were consistent with the dependence of the radiation pressure on the incident-light conditions reported in previous experiments and calculations, which support the validity of the experimental system and method for particle velocity measurement in the present study. Furthermore, the variation in the radiation pressure with the laser power and θ_i can be estimated using theoretical calculations based on $I_{e,integrated}$. For the polarization states, considering the difference in the reflection characteristics of each polarization state at the particle surface in addition to the integrated evanescent-field intensity is necessary.

D. Effects of particle size on particle velocity

The velocity of microparticles with various diameters was measured to examine the effect of particle size on the velocity measurement. The square symbols in Fig. 8 shows the U_{ave} of PS particles with a diameter of 3 – 12 μm measured in solution 0. The laser power, polarization, and θ_i were set to 507 mW, s-polarization, and 62°, respectively. It was difficult to accurately measure the velocity of 1 μm particles as they exhibited strong Brownian motion. The fluctuations of the particle positions, especially in the vertical direction, have a significant effect on the magnitude of the evanescent-field radiation pressure acting on the particle. As a result, 1 μm particles, which could not remain in the evanescent field stably, were only minimally driven by the radiation pressure. For this reason, results are presented for particles larger than 1 μm in Fig. 8. The red dotted line shows $I_{e,integrated}$ normalized by the value at $2r = 10\,\mu$m. The black dotted line shows the trend of velocity variation with particle size, which was estimated from $I_{e,integrated}$ and fitted to the measured velocity values.

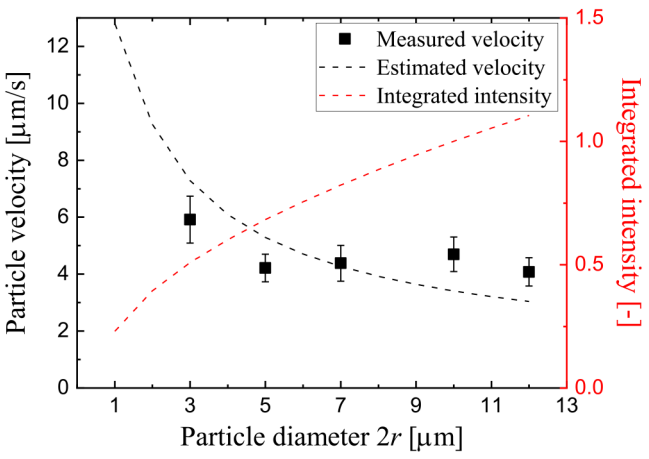

FIG. 8. Variation in the measured particle velocity U_{ave}, $I_{e,integrated}$, and estimated velocity with respect to particle diameter $2r$.

From the theoretical prediction, $I_{e,integrated}$ increased with particle size. This trend was qualitatively consistent with the previous studies that reported the radiation pressure increased with the particle size.[15,20,53] This increase is attributed to an increase in the particle surface area irradiated by the evanescent field. By contrast, the estimated velocity decreased as the particle size increased. One reason for this is that the Stokes drag force increases in proportion to the particle radius. The second reason is that d_{eq}/r decreased with increasing particle size, resulting in the lager wall effect on $F_{Stokes,mod}$; the R value increased from 2.0 to 3.4 with increasing particle diameter from 1 to 12 μm. The measurement result shows that, in the present range of particle diameter (from 3 to 12 μm), the particle velocity did not change significantly or appeared to decrease slightly with the increasing particle size; however, this was not clear because of the large error bars. The reason for the discrepancy between the theory and measurement can be the decrease of measurement accuracy for smaller particles due to the increase of the effect of Brownian motion. Therefore, to further validate the measured values presented here, the measurement of larger particle-size is required where uncertainties in the velocity measurement and d_{eq} estimation are effectively reduced. In the same sense, 10 μm particles were used in the subsequent section in which the effect of the separation distance was examined.

E. Effect of separation distance on particle velocity

The velocities of 10 μm PS particles parallel to the glass–solution interface were measured for solutions with different NaCl concentrations in the range of $0 \le C_{NaCl} \le 60$ mM. Because the ion concentration of the particle solution changes the magnitude of F_{EDL} and d_{eq}, the particle motion was expected to vary with C_{NaCl}. The laser power, polarization, and θ_i were set to 507 mW, s-polarization, and 62°, respectively.

Prior to the experiment, the effects of d_{eq} on the radiation pressure, $F_{Stokes,mod}$, and particle velocity were analyzed theoretically. Figure 9(a) shows the variations in the $F_{Stokes,mod}$ correction factor R and $I_{e,integrated}$ with respect to d_{eq}. Both values were normalized to those at $d_{eq} = 64.3$ nm (corresponding to the d_{eq} of solution 0). The upper axis of the figure shows C_{NaCl} that corresponds to d_{eq}. $I_{e,integrated}$ increased almost linearly with decreasing d_{eq}, whereas R exhibited a nonlinear increase in accordance with Eq. (12). The increase rates for both were comparable at $d_{eq} = 20 – 70$ nm; however, R increased more rapidly than $I_{e,integrated}$ as the particle approached the wall surface. Therefore, the ratio of $I_{e,integrated}$ to R, which is indicated by the black line, was almost unity at $d_{eq} > \sim 25$ nm. However, this ratio began to decrease at d_{eq}

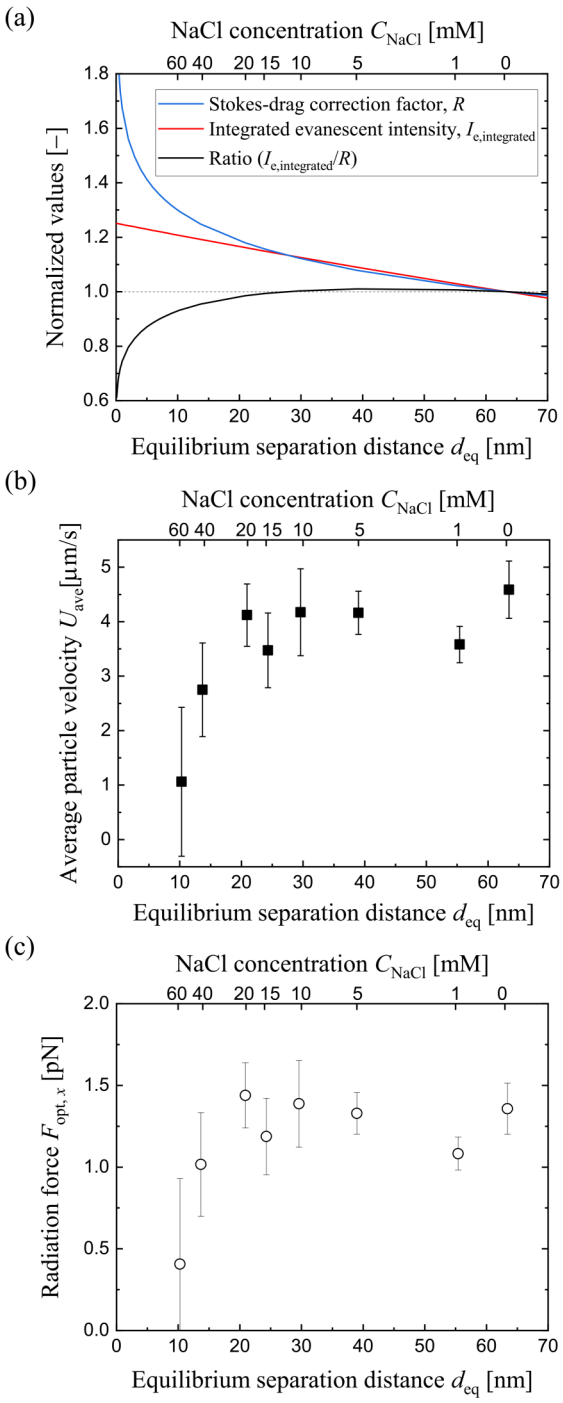

FIG. 9. (a) Variation in correction factor, R, of modified Stokes drag force, $F_{Stokes,mod}$, integrated evanescent intensity, $I_{e,integrated}$, and the ratio of the two with respect to d_{eq}. The values are normalized by those at d_{eq} = 64.3 nm (corresponding to C_{NaCl} = 0 mM). The upper axis shows C_{NaCl} that correspond to d_{eq}. (b) U_{ave} and (c) estimated radiation force, $F_{opt,x}$, for 10 μm PS particles in solutions 0–60 plotted against d_{eq}.

~25 nm and reduced to 0.6 at d_{eq} = 0.1 nm. If we assume that $F_{opt,x}$ is proportional to $I_{e,integrated}$ and that U is determined by the balance between $F_{opt,x}$ and $F_{Stokes\ mod,}$ the following relationship is obtained:

$$U(d_{eq}) = \frac{F_{opt,\,x}}{6\pi\mu r \cdot R(d_{eq})} = \frac{C_1 \cdot I_{e,integrated}(d_{eq})}{6\pi\mu r \cdot R(d_{eq})} = C_2 \frac{I_{e,integrated}(d_{eq})}{R(d_{eq})}. \quad (13)$$

Here, C_1 and C_2 are constants. From Eq. (13), the change in particle velocity with respect to d_{eq} is expected to exhibit the same distribution as the ratio of $I_{e,integrated}$ to R indicated by the black line in Fig. 9(a).

Figure 9(b) shows the velocity measurement results plotted against d_{eq}. U_{ave} was almost constant at ~4 μm/s for $d_{eq} \geq 20$ nm (corresponding to $C_{NaCl} \leq 20$ mM) and began to decrease rapidly at ~20 nm down to ~1 μm/s for d_{eq} = 10 nm (corresponding to C_{NaCl} = 60 mM). The change in U_{ave} vs d_{eq} is qualitatively consistent with the prediction indicated by the black line in Fig. 9(a). This agreement indicates that the dependence of near-wall particle velocity on d_{eq} is determined by the balance between the evanescent-field radiation force and FStokes,mod. Thus, the particle velocity was constant for $d_{eq} \geq 20$ nm because the increases in the radiation pressure and $F_{Stokes,mod}$ with decreasing d_{eq} canceled each other. Furthermore, at $d_{eq} < 20$ nm, the particle velocity decreased because the effect of the increase in $F_{Stokes,mod}$ exceeded the radiation pressure. This result indicates that the wall effect on the Stokes drag force (i.e., d_{eq} dependence of R) needs to be correctly incorporated especially in this area. The decrease in the measured velocity with decreasing d_{eq} was more rapid than that predicted theoretically for $d < 20$ nm. One possible cause of the more rapid decrease in the measured velocity is the frictional force between the particles and the wall surface. Another possible cause is the uncertainty in the estimation of d_{eq}. In other words, the actual particle position may have been closer to the wall than estimated.

Figure 9(c) shows the relationship between d_{eq} and the radiation pressure estimated from the measured velocities using Eq. (12). The radiation pressure was approximately 1.2−1.4 pN for $d_{eq} > 20$ nm. The radiation pressure was also predicted from the result of ray optics model,[20] considering the differences in θ_i and the laser intensity per unit area between our experiments and the calculations reported in Ref. 20. The measurement value of 1.2 −1.4 pN was of the same order (but approximately five times larger) as the predicted one. The discrepancy between the measurement result and prediction may have been due to several sources, including uncertainty in the estimation of d_{eq} and the approximate nature of the model.[21] In Fig. 9(c), the radiation pressure decreased rapidly for $d_{eq} < 20$ nm. As the evanescent intensity increases with decreasing z, the radiation pressure acting on the particles should monotonically increase with decreasing d_{eq}, as was the case for the $I_{e,integrated}$ distribution shown by the red line in Fig. 9(a). The difference in the trend between measured values and theoretical predictions could be attributed to the effect of friction. Surface roughness and Brownian motion of microparticles can cause contact between the particles and the wall surface, which results in

friction. Assuming that a frictional force of ~1 pN acts on the particle at $d_{eq} = 10$ nm, the calculated friction coefficient μ is 0.08, which is comparable to the friction coefficients between well-lubricated non-metals reported in the literature.[54]

These results demonstrate that the change in the magnitude of the wall effect with respect to d_{eq} needs to be correctly considered in order to accurately estimate the radiation pressure from the particle velocities and vice versa. In addition, it is desirable to conduct particle manipulation at $d_{eq} > 20$ nm because the change in R with d_{eq} and the effect of friction is particularly significant at $d_e < 20$ nm.

V. SUMMARY AND CONCLUSIONS

In this study, the motion of PS microparticles in an evanescent field was investigated experimentally and theoretically while considering the effect of the wall–particle interaction. d_{eq} was theoretically evaluated by considering the balance of the vertical forces exerted on the particles. An increase in the NaCl concentration from 0 to 60 mM, which caused a decrease in the EDL thickness and absolute values of the zeta potentials, decreased d_{eq} from 63 to 10 nm. This altered the $F_{Stokes,mod}$ correction factor from 2.7 to 4.3. That is, the magnitude of the hydrodynamic resistance acting on the particles propelled parallel to the interface was several times larger than that in the bulk and varied by a factor of 1.6 with d_{eq}.

The velocity of PS particles was measured while changing the incident-light conditions and particle size to confirm the validity of the experimental methods. We confirmed that the particles of the diameter in the range of 3–12 μm were driven parallel to the TIR interface at speeds on the order of 1 μm/s in the evanescent-wave propagation direction. The positive correlation between the particle velocity and light intensity was confirmed. As θ_i increased from θ_c, the particle velocity decreased rapidly by approximately one order of magnitude due to the decrease in both z_p and the light intensity at the TIR interface. These measurement results were consistent with the previous experiments and calculations. Furthermore, the theoretical calculation based on $I_{e,integrated}$ was found useful for approximately predicting the trend in radiation pressure variation. By contrast, the effects of polarization states and particle diameter on the measured velocity were almost indistinguishable due to the measurement error.

The effect of d_{eq} on the particle velocity was examined by using solutions with various NaCl concentrations. The velocities of 10 μm PS particles were almost constant for $20 < d_{eq} < 70$ nm but decreased rapidly below that distance. This trend was consistent with the theoretical prediction based on the dependences of $I_{e,integrated}$ and $F_{Stokes,mod}$ on d_{eq}. Thus, the constant velocity in this region can be explained by the balance between the evanescent-field radiation pressure and $F_{Stokes,mod}$. The rapid decrease in particle velocity for $d_{eq} < 20$ nm was attributed to the significant change in R with respect to d_{eq} and the friction between the wall and particles.

The experimental and theoretical results clearly detail the importance of considering the effects that the neighboring wall have on the particles through intermolecular, electrostatic, and hydrodynamic drag forces for accurate predictions and control of the microparticle motion in an evanescent field. Therefore, from an application perspective, the conditions of the solution and particle/wall surface can have considerable effects. This would be especially crucial in the fields of lab-on-a-chip and biomedical engineering because these applications involve complex samples, and thus, more complex wall-particle interactions (hydrophobic interactions, hydration forces, etc.) can be exhibited. For more accurate discussion on the wall effect, the accuracy of d_{eq} estimation should be improved. The vertical position (i.e., d_{eq}) of the particle can be estimated more accurately than the inference method used in this study by measuring the scattered light by the particles in the evanescent field.[55,56] Furthermore, future studies should examine the uncertainty in velocity measurements due to Brownian motion in more detail, as well as the effect of wall friction.

SUPPLEMENTARY MATERIAL

See the supplementary material for details of the measurement of the zeta potentials of the PS microparticles and the microparticle motions in solutions with different ion concentrations.

ACKNOWLEDGMENTS

This work was partially supported by a JSPS Grant-in-Aid for Early-Career Scientists (Grant No. JP18K13701).

AUTHOR DECLARATIONS

Conflict of Interest

The authors have no conflicts to disclose.

Author Contributions

Reiko Kuriyama: Conceptualization (equal); Data curation (equal); Formal analysis (equal); Funding acquisition (equal); Investigation (equal); Methodology (equal); Project administration (equal); Software (equal); Validation (equal); Visualization (equal); Writing – original draft (equal). **Miyu Inoue:** Formal analysis (equal); Investigation (lead); Methodology (equal); Software (equal); Visualization (equal). **Daiki Arita:** Formal analysis (equal); Investigation (equal); Methodology (equal); Software (equal); Visualization (equal). **Kazuya Tatsumi:** Conceptualization (equal); Supervision (equal); Writing – original draft (equal); Writing – review & editing (equal).

DATA AVAILABILITY

The data that support the findings of this study are available within the article and its supplementary material.

REFERENCES

[1]D. Axelrod, *Chapter 7 in Methods in Cell Biology* (Academic Press, 2008), Vol. 89, pp. 169–221.
[2]M. L. Martin-Fernandez, C. J. Tynan, and S. E. D. Webb, J. Microsc. **252**(1), 16–22 (2013).
[3]H. Raether, *Surface Plasmons on Smooth and Rough Surfaces and on Gratings, Springer Tracts in Modern Physics* (Springer, Berlin, 1988), Vol. III.
[4]R. C. Reddick, R. J. Warmack, D. W. Chilcott, S. L. Sharp, and T. L. Ferrell, Rev. Sci. Instrum. **61**(12), 3669–3677 (1990).
[5]T. L. Ferrell, T. A. Callcott, and R. J. Warmack, Am. Sci. **73**(4), 344–353 (1985).

[6]A. Ashkin, J. M. Dziedzic, J. E. Bjorkholm, and S. Chu, Opt. Lett. **11**(5), 288 (1986).
[7]A. Ashkin and J. M. Dziedzic, Science **235**(4795), 1517–1520 (1987).
[8]A. Ashkin, J. M. Dziedzic, and T. Yamane, Nature **330**(6150), 769–771 (1987).
[9]C. Bustamante, Z. Bryant, and S. B. Smith, Nature **421**(6921), 423–427 (2003).
[10]A. Ishijima and T. Yanagida, Trends Biochem. Sci. **26**(7), 438–444 (2001).
[11]S. Kawata and T. Sugiura, Opt. Lett. **17**(11), 772–774 (1992).
[12]S. Kawata and T. Tani, Opt. Lett. **21**(21), 1768–1770 (1996).
[13]T. Tanaka and S. Yamamoto, Appl. Phys. Lett. **77**(20), 3131–3133 (2000).
[14]S. Gaugiran, S. Gétin, J. M. Fedeli, G. Colas, A. Fuchs, F. Chatelain, and J. Dérouard, Opt. Express **13**(18), 6956–6963 (2005).
[15]R. F. Marchington, M. Mazilu, S. Kuriakose, V. Garcés-Chávez, P. J. Reece, T. F. Krauss, M. Gu, and K. Dholakia, Opt. Express **16**(6), 3712–3726 (2008).
[16]G. Brambilla, G. S. Murugan, J. S. Wilkinson, and D. J. Richardson, Opt. Lett. **32**(20), 3041–3043 (2007).
[17]S. Chang, J. H. Jo, and S. S. Lee, Opt. Commun. **108**(1–3), 133–143 (1994).
[18]J. P. Barton, D. R. Alexander, and S. A. Schaub, J. Appl. Phys. **66**(10), 4594–4602 (1989).
[19]E. Almaas and I. Brevik, J. Opt. Soc. Am. B **12**(12), 2429 (1995).
[20]J. Y. Walz, Appl. Opt. **38**(25), 5319–5330 (1999).
[21]R. J. Oetama and J. Y. Walz, Colloids Surf. A **211**(2–3), 179–195 (2002).
[22]L. P. Ghislain, N. A. Switz, and W. W. Webb, Rev. Sci. Instrum. **65**, 2762–2768 (1994).
[23]Y. Harada and T. Asakura, Opt. Commun. **124**(5–6), 529–541 (1996).
[24]V. Garcés-Chávez, K. Dholakia, and G. C. Spalding, Appl. Phys. Lett. **86**, 031106 (2005).
[25]M. Šiler, T. Čižmár, M. Šerý, and P. Zemánek, Appl. Phys. B **84**, 157–165 (2006).
[26]T. Čižmár, M. Šiler, M. Šerý, P. Zemánek, V. Garcés-Chávez, and K. Dholakia, Phys. Rev. B **74**, 035105 (2006).
[27]X. Han, H. Luo, G. Xiao, and P. H. Jones, Opt. Lett. **41**(21), 4935–4938 (2016).
[28]Ş Arslanyürek and M. S. Dinleyici, Opt. Commun. **562**, 130543 (2024).
[29]P. J. Reece, V. Garcés-Chávez, and K. Dholakia, Appl. Phys. Lett. **88**, 221116 (2006).
[30]V. Garcés-Chávez, R. Quidant, P. J. Reece, G. Badenes, L. Torner, and K. Dholakia, Phys. Rev. B **73**, 085417 (2006).
[31]M. Righini, A. S. Zelenina, C. Girard, and R. Quidant, Nat. Phys. **3**, 477–480 (2007).
[32]M. Righini, G. Volpe, C. Girard, D. Petrov, and R. Quidant, Phys. Rev. Lett. **100**, 186804 (2008).
[33]S. Rezaei, D. Azami, F. Kheirandish, and A. Hassanzadeh, J. Opt. Soc. Am. A **39**(11), 2054–2062 (2022).
[34]O. V. Angelsky, C. Y. Zenkova, S. G. Hanson, and J. Zheng, Front. Phys. **8**, 159 (2020).
[35]P. Paiè, T. Zandrini, R. M. Vázquez, R. Osellame, and F. Bragheri, Micromachines **9**, 200 (2018).
[36]P. Praveen Kamath, S. Sil, V. G. Truong, and S. Nic Chormaic, Biomed. Opt. Express **14**(12), 6172–6189 (2023).
[37]A. C. Svistun, E. V. Musafirov, and D. V. Guzatov, J. Appl. Spectrosc. **91**(4), 761–768 (2024).
[38]G. Tkachenko, V. G. Truong, C. L. Esporlas, I. Sanskriti, and S. Nic Chormaic, Nat. Commun. **14**, 1691 (2023).
[39]P. H. Jones, O. M. Maragò, and G. Volpe, *Optical Tweezers: Principles and Applications* (Cambridge University Press, 2015).
[40]D. C. Prieve and J. Y. Walz, Appl. Opt. **32**(9), 1629–1641 (1993).
[41]B. J. Kirby and E. F. Hasselbrink, Jr., Electrophoresis **25**(2), 187–202 (2004).
[42]H. C. Hamaker, Physica **4**(10), 1058–1072 (1937).
[43]Y. Gu and D. J. Li, J. Colloid Interface Sci. **217**(1), 60–69 (1999).
[44]E. W. K. Young and D. Li, Langmuir **21**(25), 12037–12046 (2005).
[45]R. Hogg, T. W. Healy, and D. W. Fuerstenau, Trans. Faraday Soc. **62**, 1638 (1966).
[46]J. N. Israelachvili and D. Tabor, Proc. R. Soc. London, Ser. A **331**, 39–55 (1972).
[47]J. N. Israelachvili, *Intermolecular and Surface Forces*, 3rd ed. (Academic Press, 2011).
[48]A. J. Goldman, R. G. Cox, and H. Brenner, Chem. Eng. Sci. **22**(4), 637–651 (1967).
[49]T. Cao, M. Borkovec, and G. Trefalt, Colloids Interfaces **4**(4), 52 (2020).
[50]F. M. Sogandares and E. S. Fry, Appl. Opt. **36**(33), 8699–8709 (1997).
[51]HOYA GROUP Optics Division, see http://www.hoya-opticalworld.com for the absorption coefficient of BK7 glass.
[52]H. Mao, J. Ricardo Arias-Gonalez, W. B. Smith, I. Tinoco, Jr., and C. Bustamante, Biophys. J. **89**(2), 1308–1316 (2005).
[53]D. Ganic, X. Gan, and M. Gu, Opt. Express **12**(22), 5533–5538 (2004).
[54]M. Besanconr, *The Encyclopedia of Physics*, 2nd ed. (Van Nostrand Reinhold Company, New York, 1974), p. 376.
[55]J. Y. Walz, Curr. Opin. Colloid Interface Sci. **2**(6), 600–606 (1997).
[56]S. G. Bike, Curr. Opin. Colloid Interface Sci. **5**(1–2), 144–150 (2000).